Geophys. J. R. astr. Soc. (1979) **58**, 689–715

Finite deformation during fluid flow

Dan McKenzie *Department of Geodesy and Geophysics, Madingley Rise, Madingley Road, Cambridge CB3 0EZ*

Received 1979 February 5; in original form 1978 April 4

Summary. Typical upper mantle circulations obtained by solving Stokes' equation produce finite deformations which differ in important ways from those produced by pure or simple shear. Finite strain, defined by the ratio of the long to the short axis of the deformation ellipse, in most cases shows a steady increase with superimposed oscillations. Similarity solutions for the flow near plate boundaries demonstrate that the observed seismic anisotropy in the oceanic lithosphere can be produced by the finite deformation beneath the ridge axes. The same mechanism should give rise to strong anisotropy in the mantle above sinking slabs. Such anisotropy has not yet been detected, perhaps because the observed high velocities have been attributed to thermal effects. Convection in the mantle remote from plate boundaries produces complicated deformation which varies rapidly with position and will therefore be difficult to map seismically. The fabrics of nodules in lavas and kimberlites suggest that large strains can occur in the mantle under stresses which are too small to produce dislocation movement. The large and complicated finite deformation produced by the convective circulation in the mantle also affects closed geochemical systems, and leads to thorough mixing of any convecting region.

1 Introduction

A number of attempts have recently been made to use observed plate motions and other instantaneous observations as constraints on the form of mantle circulation. The principal difficulty such investigations have faced is the limited number of relevant observations and not the calculation of the corresponding properties of the models. Little use has yet been made of geochemical and structural observations made on samples of mantle material brought up by basalt and kimberlite magmas, or of observations of seismic anisotropy, yet some of this information could be directly relevant to mantle convection. It is, however, much less straightforward to calculate the corresponding properties of the models for comparison with the observations because the entire history of the motion of a piece of rock is involved, rather than its present instantaneous deformation. A description of fluid flow in terms of the particle paths of individual fluid elements is known as a Lagrangian description,

and is rarely used in fluid mechanics because of the difficulties which arise in imposing boundary conditions. To investigate problems involving observations of rock fabric, seismic anisotropy or geochemistry it is necessary first to obtain the solution to the fluid dynamical problem in a reference frame fixed to the boundaries, called the Eulerian description, then to convert this to a Lagrangian description, then finally to investigate the deformation. This paper is principally concerned with the problems of making such calculations. To complete the model calculations requires a theory which can relate a general time-dependent deformation to the resulting fabric and a theory of magma segregation from a dispersed partial melt. At present neither theory is available, although certain plausible statements can be made (see Sections 6–8).

An attempt has been made to separate the purely mathematical part of the problem (Sections 2–5) from the parts relevant to the Earth (Sections 6–8), but inevitably the two are closely connected.

To investigate the finite deformation some model of mantle circulation is required, and that used here as a guide is compatible with a variety of geophysical and fluid mechanical arguments (Richter & McKenzie 1978; Parsons & McKenzie 1978). In this model the flow consists of two parts. A large-scale flow returns material from the trenches to the ridges. Beneath the interior of large plates this flow involves no vertical motions and is simple shear. Beneath plate boundaries the flow resembles the similarity solutions discussed in Section 4. In addition to this large-scale flow, heat is transported vertically by a small-scale circulation whose plan form is unknown, although it may consist of rolls aligned along the shear direction. Most numerical experiments on convecting fluids are relevant to the small-scale circulation. Both the large- and small-scale circulations are restricted to the outer 700 km of the Earth. Although this model is used as a guide to the investigations of finite strain discussed below, it contains a wide variety of types of deformation. Hence the results can easily be used to investigate the deformation associated with other convective models, such as whole mantle convection or models without small-scale flow. The only class of models which have not been examined are those with time dependence. These are slightly more difficult to investigate than the steady state flows discussed below because the particle paths are not stream lines. Apart from this complication the same methods described in Section 2 could be used.

2 Finite deformation

We need to be able to relate the vector $\mathbf{y}'(t)$ which joins two particles in a fluid element at positions $\mathbf{x}_1'(t)$ and $\mathbf{x}_2'(t)$, to $\mathbf{y}$ the vector joining the same two particles at $t = 0$

$$\mathbf{y}'(t) = \mathcal{F}(t)\mathbf{y}. \tag{1}$$

The matrix $\mathcal{F}$ is initially the unit matrix $\mathcal{I}$. The shape of any body at time t, represented by a sequence of vectors $\mathbf{z}_n$ at $t = 0$ can be determined by matrix multiplication from equation (1) provided $\mathcal{F}(t)$ is known. The algebra in this section is concerned with the relationship between $\mathcal{F}$ and the Eulerian velocity field, and with how $\mathcal{F}$ can be obtained from this relationship. The notation and development follows that of Malvern (1969). None of the formulations adopted by other authors (Jaeger 1962; Dieterich & Onat 1969; Elliott 1972) is easily adapted to the rather complicated circulations considered below. At time t

$$\mathbf{y}'(t) = \mathbf{x}_2'(t) - \mathbf{x}_1'(t) \tag{2}$$

at a later time $t + \delta t$

$$\mathbf{y}'(t + \delta t) = \mathbf{x}_2'(t + \delta t) - \mathbf{x}_1'(t + \delta t) \tag{3}$$

subtracting and taking the limit as $\delta t \to 0$ gives

$$D_t \mathbf{y}' = \mathbf{v}'(\mathbf{x}_2', t) - \mathbf{v}'(\mathbf{x}_1', t) \tag{4}$$

where $\mathbf{v}'(\mathbf{x}', t)$ is the velocity of the fluid at position $\mathbf{x}'$ and time t, and D_t is the Lagrangian derivative. Provided the size of the fluid element is small compared with the scale of the flow $\mathbf{v}'(\mathbf{x}_2, t)$ can be expanded as a Taylor series, giving

$$D_t y_i' = \left(\frac{\partial v_i'}{\partial x_k'}\right)_{\mathbf{x}', t} y_k' = L_{ik} y_k' \tag{5}$$

where summation over repeated subscripts is implied. Malvern calls L_{ik} the velocity gradient tensor, and it can be obtained by differentiation from the usual Eulerian description of the motion. Substitution of equation (1) into equation (5) gives

$$D_t F_{ij} = L_{ik} F_{kj}. \tag{6}$$

Hence $\mathscr{F}$ can be determined by integrating equation (6), subject to an initial condition $\mathscr{F}(0) = \mathscr{I}$. $\mathscr{F}(t)$ in general depends on the position of the fluid element at $t = 0$ and $\mathscr{L}$ must be evaluated at the position $\mathbf{x}'$ of the element at time t. Since element paths are stream lines if the flow is two-dimensional and time independent, $\mathscr{F}$ is simpler to obtain for steady circulations than it is for time-dependent ones. For this reason all cases considered below are steady flows.

Equation (6) and the initial conditions form a complete statement of the mathematical problem. However, analytic integration of equation (6) is straightforward only for the simplest flows where $\mathscr{L}$ is independent of both position and time. Some two-dimensional examples of such circulations are considered in Section 3. When this condition is not satisfied it is generally more straightforward to integrate equation (6) numerically. Numerical integration can be carried out in various ways. If analytic expressions for L_{ik} and the velocity field are available then the Runge–Kutta–Gill method is the obvious choice, since the initial condition alone is known. However, when L_{ik} and the velocity field have been obtained numerically it is not possible to choose constant time intervals for integration, and other methods must be used.

The time derivative in equation (6) is the Lagrangian derivative, hence if the integration is carried out along a particle path the advection terms are zero. If F_{ij} at time $n\Delta t$ is written F_{ij}^n, equation (6) can be written in finite difference form as

$$\frac{F_{ij}^{n+1} - F_{ij}^n}{\Delta t} = L_{ik}(F_{kj}^{n+1} + F_{kj}^n)/2. \tag{7}$$

Such a scheme is properly centred in time. Equation (7) can be rearranged to give

$$\mathscr{F}^{n+1} = \mathscr{A}^{-1}\mathscr{B}\mathscr{F}^n \tag{8}$$

where

$$A_{ij} = \delta_{ij} - \frac{\Delta t}{2} L_{ij} \tag{9}$$

$$B_{ij} = \delta_{ij} + \frac{\Delta t}{2} L_{ij}. \tag{10}$$

Equation (8) is accurate to $O(\Delta t^2)$. Of particular importance is whether the numerical scheme conserves material, since a surface enclosing a unit volume in an incompressible

fluid at time $t = 0$ should do so at all later times. It is straightforward to show that the volume enclosed is given by $\det(\mathscr{F}^n)$, the determinant of $\mathscr{F}^n$, and that equation (8) gives

$$\det(F_{ij}^{n+1}) = (1 + O(\Delta t)^3) \det(F_{ij}^n) \tag{11}$$

when

$$\frac{\partial v_l}{\partial x_l} = 0. \tag{12}$$

Furthermore when the deformation is confined to two dimensions, terms in Δt^3 vanish and the numerical scheme conserves area exactly.

An alternative method of integrating equation (6) is to write the Lagrangian derivative in Eulerian form

$$D_t F_{ij} = \left(\partial_t + v_l \frac{\partial}{\partial x_l}\right) F_{ij} = L_{ik} F_{kj}. \tag{13}$$

Equation (13) may then be solved in two dimensions by methods similar to those used for thermal convection calculations. Using a square mesh of spacing Δx and integrating over a square box of side $2\Delta x$ centred on the grid point l, m gives

$$\begin{aligned}\mathscr{F}_{l,m}^{n+1} = \mathscr{A}_{l,m}^{-1} \mathscr{B}_{l,m} \mathscr{F}_{l,m}^n - \frac{\Delta t}{2\Delta x} \mathscr{A}_{l,m}^{-1} (&v_{l,m+1} \mathscr{F}_{l,m+1}^{n+\frac{1}{2}} - v_{l,m-1} \mathscr{F}_{l,m-1}^{n+\frac{1}{2}} \\ &+ u_{l+1,m} \mathscr{F}_{l+1,m}^{n+\frac{1}{2}} - u_{l-1,m} \mathscr{F}_{l-1,m}^{n+\frac{1}{2}})\end{aligned} \tag{14}$$

where u and v are the x and y components of the velocity. The use of two meshes, one for $\mathscr{F}^n$, $\mathscr{F}^{n+1}, \ldots$, the other for $\mathscr{F}^{n+\frac{1}{2}}$, $\mathscr{F}^{n+3/2}, \ldots$, allows the difference scheme to be properly centred in space and time. The usual Courant–Friedrich–Lewy condition was imposed on the time step to ensure stability. One important difference between equation (14) and the corresponding equation governing the temperature in a convecting fluid is that no steady state solution to equation (14) exists. When $(u, v) = 0$ and $\mathscr{A}^{-1}\mathscr{B}$ is constant $\mathscr{F}$ grows exponentially with time (Section 3). Solutions to equation (14) behave in a more complicated way, and short wavelength variations which are not properly resolved by the mesh have complex growth rates with positive real parts. Since mesh points with $l + m$ odd are independent of those with $l + m$ even propagation of short wavelength errors produces oscillations in $\mathscr{F}_{l,m}$. This behaviour was suppressed by introducing a small diffusion term.

With the exception of equation (14) the general theory above applies to any three-dimensional deformation, and can be considerably simplified if the deformation is produced by two-dimensional steady flows. Since the fluid is incompressible the velocity may be written in terms of a stream function ψ:

$$\mathbf{v} = (\partial_y \psi, -\partial_x \psi, 0). \tag{15}$$

Hence in two dimensions

$$\mathscr{L} = \begin{bmatrix} \partial_x \partial_y \psi, & \partial_y^2 \psi \\ \partial_x^2 \psi, & -\partial_x \partial_y \psi \end{bmatrix}. \tag{16}$$

It is convenient to separate $\mathscr{L}$ into antisymmetric $\mathscr{C}$ and symmetric $\mathscr{S}$ parts. In three dimensions

$$C_{ik} = \tfrac{1}{2} \epsilon_{ijk} \omega_j \tag{17}$$

where ϵ_{ijk} is the alternating tensor and $\boldsymbol{\omega} = \nabla \times \mathbf{v}$ is the vorticity. In two dimensions the vorticity is a scalar, ω, and

$$\mathscr{C} = \begin{bmatrix} 0 & -\omega/2 \\ \omega/2 & 0 \end{bmatrix} \tag{18}$$

where

$$\omega = -\partial_x^2\psi - \partial_y^2\psi. \tag{19}$$

The vorticity is obtained during the integration of the equations governing thermal convection, and hence equation (18) is easily evaluated. The symmetric part of $\mathscr{L}$ is

$$\mathscr{S} = \begin{bmatrix} \partial_x\partial_y\psi, & \tfrac{1}{2}(\partial_y^2\psi - \partial_x^2\psi) \\ \tfrac{1}{2}(\partial_y^2\psi - \partial_x^2\psi), & -\partial_x\partial_y\psi \end{bmatrix}. \tag{20}$$

The time δt taken for the element to travel a distance δs along the stream line is

$$\delta t = \delta s/[(\partial_x\psi)^2 + (\partial_y\psi)^2]^{1/2}. \tag{21}$$

Using equation (8) or (14) and (18), (20) and (21) $F_{ij}(t)$ can easily be evaluated from either numerical values or analytic expressions of ψ. All the examples considered in Sections 4 and 5 are obtained from these expressions.

The analysis above has been concerned with obtaining $\mathscr{F}$ and not with interpreting this matrix in terms of possible geological observations. For such an interpretation it is convenient to define some measure of the finite strain which has deformed an element of fluid. It is easy to show that any two-dimensional deformation described by $\mathscr{F}$ converts an initially circular element of fluid into an elliptical one. If the major and minor semiaxes of the ellipse are a and b respectively, a convenient definition of the finite strain f is

$$f = \log_{10}(a/b) \tag{22}$$

since $f = 0$ when $a = b$. Expressing a/b in terms of the elements of $\mathscr{F}$ gives

$$a/b = \gamma + (\gamma^2 - 1)^{1/2} \tag{23}$$

where

$$\gamma = (F_{11}^2 + F_{12}^2 + F_{21}^2 + F_{22}^2)/2. \tag{24}$$

f is closely related to the natural strain, $\log_e(a/b)$. The orientation of a and b can also be obtained from $\mathscr{F}$. If

$$\tan\theta = y_2'/y_1'$$

where $\mathbf{y}' = (y_1', y_2')$ is given by equation (1), the orientation of the two semiaxes are given by

$$\tan 2\theta = \frac{2(F_{11}F_{12} + F_{21}F_{22})}{F_{11}^2 - F_{12}^2 + F_{21}^2 - F_{22}^2}. \tag{25}$$

The two solutions for θ differ by $\pi/2$.

3 A simple example

A simple type of deformation which has been widely discussed in the geological literature is that of progressive pure shear (see Hobbs, Means & Williams 1976). If the orientation of

the direction of greatest extension is at 45° to the x axis, then the expression for $\mathscr{L}$ is

$$\mathscr{L}=\begin{bmatrix}0 & S\\ S & 0\end{bmatrix} \tag{26}$$

where S is a constant which is taken to be independent of time. The most commonly used definition of pure shear is that the vorticity of the fluid must be zero. This definition requires an external frame of reference. For our purposes it is more useful to define progressive pure shear as that deformation which does not change the direction of a vector which initially points along the direction of greatest instantaneous extension. This definition avoids all reference to external frames, since progressive pure shear is then defined in terms of the symmetric part of $\mathscr{L}$. A more general deformation than equation (26) which includes rotation is

$$\mathscr{L}=\begin{bmatrix}0, & S-W\\ S+W, & 0\end{bmatrix} \tag{27}$$

where W is the instantaneous angular velocity about the $+z$ axis in a positive screw sense, and the vorticity is $2W$. As before the x and y axes are related to the symmetric part of $\mathscr{L}$. In this case equation (6) can be solved analytically in a frame in which $\mathbf{v}=0$:

$$\mathscr{F}=\begin{bmatrix}\cosh nt, & \left(\dfrac{S-W}{S+W}\right)^{1/2}\sinh nt\\ \left(\dfrac{S+W}{S-W}\right)^{1/2}\sinh nt, & \cosh nt\end{bmatrix} \tag{28}$$

where $n^2=S^2-W^2>0$.

$$\mathscr{F}=\begin{bmatrix}1, & 0\\ (S+W)t, & 1\end{bmatrix} \tag{29}$$

if $S=W$, and

$$\mathscr{F}=\begin{bmatrix}\cos \Omega t, & -\left(\dfrac{W-S}{W+S}\right)^{1/2}\sin \Omega t\\ \left(\dfrac{W+S}{W-S}\right)^{1/2}\sin \Omega t, & \cos \Omega t\end{bmatrix} \tag{30}$$

where $\Omega^2=W^2-S^2>0$. Equation (28) corresponds to progressive pure shear when $W=0$. Equation (29) can be obtained from either equation (30) or equation (28) by allowing W to approach S, and describes progressive simple shear when the flow is parallel to the y axis. Fig. 1(b) shows the strain as a function of time for $S=1$ and for four values of W, obtained from equations (22) and (28)–(30). It is obvious that the finite strain depends on both W and S. For values of $|W|$ less than S the behaviour of $f(t)$ is similar to that of pure shear and, after sufficient time, f increases linearly with t. Progressive simple shear is a special case which requires $|W|=S$ for all time, and f increases monotonically as $\log_{10} t$. When $|W|>S$, f is oscillatory. This behaviour is to be expected from equation (30), since f must be zero when $\sin \Omega\tau=0$ and $\tau=n\pi/\Omega$, where n is an integer and Ω is the period. Fig. 1 shows that, provided $S>|W|$, rotation does not produce oscillatory behaviour in f. When $|W|>S$,

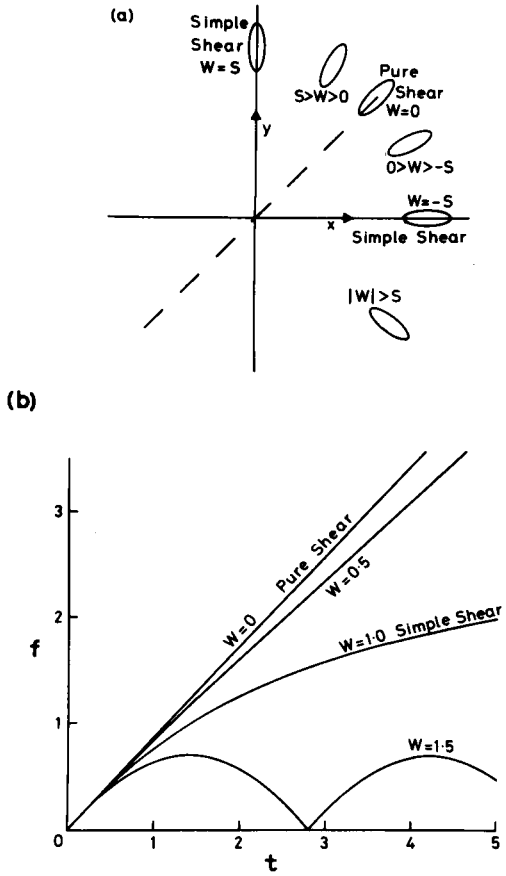

Figure 1. (a) Sketch to show the type of deformation produced by equations (28)–(30). The direction of maximum instantaneous extension is shown as a dashed line and, when $W = 0$, vectors pointing in this direction are not rotated. The greater principal axis of the ellipse, a, lies in the same direction. When $S > |W| > 0$ a lies in the positive quadrant. When $W = S$ or $W = -S$ the invariant vectors lie along the y or x axes. The only cases for which a can lie in the $+x$, $-y$ quadrant occur if $|W| > S$ and then only for some of the time. (b) The strain $f(t)$ from equation (22) for four cases, obtained from equations (28)–(30) and (22)–(24).

f does oscillate, but with a period which depends on both the rotation and the pure shear rates. Similar behaviour occurs in more complicated cases discussed below.

One question of some interest is whether the deformation described by equation (27) leaves the direction of any vector x unchanged. This question is easily answered using equation (28). If $\theta = y/x$ and $\theta' = y'/x'$ substitution of equation (28) into equation (1) gives

$$\theta'\theta\left(\frac{S-W}{S+W}\right)^{1/2}\sinh nt + (\theta' - \theta)\cosh nt = \left(\frac{S+W}{S-W}\right)^{1/2}\sinh nt. \tag{31}$$

Putting $\theta = \theta'$ gives

$$\theta = \pm\left(\frac{S+W}{S-W}\right)^{1/2}. \tag{32}$$

Therefore two initial directions remain unchanged. These directions are only at right angles, with one aligned along the direction of maximum instantaneous extension, when $W = 0$.

For other values of W these two directions are symmetrical about the y axis, coinciding with it when $W = S$. When $W > S$ equation (32) has no real solution, hence the deformation rotates all vectors.

Perhaps the most surprising feature of these results is the wide range of values of W which result in deformation similar to that of progressive pure shear. Simple shearing, however, is a special type of deformation which occurs only for two values of W, $\pm S$. As perhaps might be expected from these results, none of the more general circulations discussed below resemble simple shearing. The commonest type of behaviour is similar to equation (30) and occurs when $|W| > S$. The principal difference between $f(t)$ obtained from equation (30) and Fig. 1 and that for more general flows arises because of spatial variations of both W and S, which prevent f returning to zero once the deformation has started. The oscillating behaviour of f occurs because the vorticity of most flows in fluid mechanics is substantial compared with the symmetric part of the deformation tensor. These examples clearly show the importance of vorticity during finite deformation.

The only part of the circulation in the mantle to which these results are relevant is the interior part of the large-scale flow. Far from plate boundaries this consists of progressive simple shear. If Richter & McKenzie's (1978) model is used the shearing in the low viscosity layer is much more rapid than that in the deeper more viscous layer. If the plate velocity is 100 mm/yr and the low viscosity layer is 50 km thick the curve marked 'simple shear' in Fig. 1 describes the strain if each division of the time axis corresponds to 1 Myr. In the more viscous layer the strain varies with depth, but the same curve describes the fastest rate of strain accumulation if each division of the time axis corresponds to about 100 Myr.

4 Some similarity solutions

Various authors (McKenzie 1969; Lachenbruch 1976) have used a similarity solution for two-dimensional Stokes flow in a corner, given by Batchelor (1967), to discuss the stress and stream lines near ridges and trenches. All such solutions have stress singularities in the corner, although no singularity occurs within the Earth because the flow ceases to obey Stokes' equation when power law creep occurs at large stresses. Despite this difficulty the similarity solutions are useful because they approximately describe the flow field near two important types of plate boundaries. In these regions the geometry of the plate motions themselves produce large finite strains, and it is of interest to know the magnitude of the resulting strain and its orientation. Such calculations are the first stage in understanding how the fabric of the rock and its velocity anisotropy are produced in such regions.

We need solutions to Stokes' equation in the absence of buoyancy forces

$$\nabla^4 \psi = 0 \tag{33}$$

in cylindrical coordinates for the geometry shown in Fig. 2. Batchelor (1967) gives the general solution to equation (33):

$$\psi = r\Theta = r(A \sin\theta + B\cos\theta + C\theta\sin\theta + D\theta\cos\theta)$$
$$\mathbf{v} = (0, v_r, v_\theta) = (0, d_\theta\Theta, -\Theta). \tag{34}$$

We shall consider the four cases for which the boundary conditions and coefficients are given in Table 1. The first case, (a), has stream lines which are symmetric about boundary 1, and boundary 2 moves at constant velocity in the $+x$ direction in Fig. 2. This solution is appropriate for a ridge axis. In the second solution, (b), boundary 1 is stress free but 2 moves at constant velocity in the radial direction. This solution is appropriate for the region above a sinking slab, equivalent to 2, when the back arc basin has no strength, or when the

Table 1. Constant coefficients in similarity solution, equation (34).

	Boundary conditions on boundary					
	1	2	A	B	C	D
(a)	$\sigma_{r\theta} = 0$	$v = v_x$	$\dfrac{2v_x \cos^2 \alpha}{2\alpha - \sin 2\alpha}$	0	0	$\dfrac{-2v_x}{2\alpha - \sin 2\alpha}$
(b)	$\sigma_{r\theta} = 0$	$v = v_r$	$\dfrac{2v_r \alpha \cos \alpha}{2\alpha - \sin 2\alpha}$	0	0	$\dfrac{-2v_r}{2\alpha - \sin 2\alpha}$
(c)	$v = 0$	$v = v_r$	$\dfrac{v_r \alpha \sin \alpha}{\alpha^2 - \sin^2 \alpha}$	0	$\dfrac{v_r(\alpha \cos \alpha - \sin \alpha)}{\alpha^2 - \sin^2 \alpha}$	$\dfrac{v_r \alpha \sin \alpha}{\alpha^2 - \sin^2 \alpha}$
(d)	$v = v_r$	$v = -v_r$	$\dfrac{v_r \alpha}{\alpha + \sin \alpha}$	0	$\dfrac{-v_r(1 + \cos \alpha)}{\alpha + \sin \alpha}$	$\dfrac{v_r \sin \alpha}{\alpha + \sin \alpha}$

v_r is the velocity in the outward radial direction in Fig. 2, v_x that in the x direction.

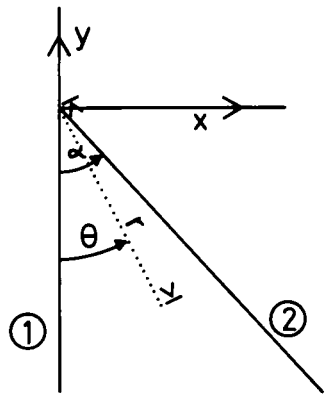

Figure 2. The geometry of the similarity solutions, see Table 1. Only the sector between boundaries 1 and 2 contains fluid, and 2 moves rigidly.

flow is decoupled from the lithosphere by a thin low viscosity layer. This can easily be seen by viewing Fig. 2 with the y axis, rather than the x axis, horizontal. Solution (c) is appropriate when the plate behind the arc does not deform. The last solution (d) is appropriate for the region beneath the plate being consumed and beneath the sinking slab, provided $\alpha > 90°$ and Fig. 2 is viewed with boundary 2 horizontal.

To obtain $\mathscr{F}(t)$ we need the vorticity ω about the z axis

$$\omega = -\frac{1}{r}(d_\theta^2 \Theta + 1) = \frac{2}{r}(D \sin \theta - C \cos \theta) \tag{35}$$

and the symmetric part of $\mathscr{L}$ (see McKenzie 1969) is

$$\mathscr{S} = \frac{1}{2r}(d_\theta^2 \Theta + 1)\begin{bmatrix} 0, & 1 \\ 1, & 0 \end{bmatrix} = \tfrac{1}{2}\begin{bmatrix} 0, & -\omega \\ -\omega, & 0 \end{bmatrix} \tag{36}$$

where $\mathscr{S}$ is expressed in cylindrical, not Cartesian, coordinates. Hence

$$\mathscr{L} = \begin{bmatrix} 0, & -\omega \\ 0, & 0 \end{bmatrix}. \tag{37}$$

At first sight equation (37) resembles equation (27) when $S = -W$, an example of simple shear. However this is not the case. $\mathscr{L}$ only has the simple form of equation (37) in cylindrical coordinates. Rotation through $-(90-\theta)$ to transform $\mathscr{L}$ to Cartesian coordinates gives

$$\mathscr{L}_c = \mathscr{R}\,\mathscr{L}\,\mathscr{R}^T = \omega\begin{bmatrix} -\sin\theta\cos\theta, & -\sin^2\theta \\ \cos^2\theta, & \sin\theta\cos\theta \end{bmatrix} \tag{38}$$

where

$$\mathscr{R} = \begin{bmatrix} \sin\theta, & \cos\theta \\ -\cos\theta, & \sin\theta \end{bmatrix} \tag{39}$$

and transforms from Cartesian to cylindrical coordinates. Since the vorticity is a function of both r and θ it is clear that substitution of equation (38) into equation (6) does not lead to an equation for $\mathscr{F}$ which is easily integrated. One simplification is, however, possible. Since the time derivative must be taken along a particle path, and hence a stream line, it may be transformed to an angular derivative:

$$\frac{D}{Dt} = |v|\frac{d}{ds} = [(d_\theta\Theta)^2 + \Theta^2]^{1/2}\frac{d}{ds} \tag{40}$$

where ds is an infinitesimal distance along a stream line

$$ds^2 = dr^2 + r^2 d\theta^2. \tag{41}$$

Since the path must be a stream line

$$d\psi = 0 = r d_\theta\Theta d\theta + \Theta dr. \tag{42}$$

Hence equation (41) becomes

$$ds = \frac{r}{\Theta}[(d_\theta\Theta)^2 + \Theta^2]^{1/2}\,d\theta \tag{43}$$

and

$$\frac{D}{Dt} = \frac{\Theta}{r}\frac{d}{d\theta}. \tag{44}$$

Equation (6) now may be written

$$d_\theta\mathscr{F} = -\frac{(d_\theta^2\Theta + 1)}{\Theta}\begin{bmatrix} -\sin\theta\cos\theta, & -\sin^2\theta \\ \cos^2\theta, & \sin\theta\cos\theta \end{bmatrix}\mathscr{F}. \tag{45}$$

To solve the problem analytically we must integrate equation (45) with initial conditions $\mathscr{F} = \mathscr{I}$ at $\theta = \theta_0$. Such integration is not straightforward, and is not attempted here. One important result is, however, obvious by inspection of equation (45). Since r does not appear on either side, $\mathscr{F}$ can only be a function of θ. Hence $\mathscr{F} = \mathscr{F}(\theta_0, \theta)$ and therefore $f = f(\theta_0, \theta)$.

This result is of particular interest for case (a), since no deformation of the fluid occurs when $\theta > \alpha$. Hence all fluid elements which start on $\theta = \theta_0$ at any value of r will have been deformed in precisely the same way when they reach $\theta = \alpha$. This result is a consequence of the existence of a similarity solution and is of considerable importance (see Section 7).

Since the analytical solution of equation (45) is not straightforward $\mathscr{F}$ and f are obtained from equations (35) and (36) for the four cases using the numerical methods discussed in

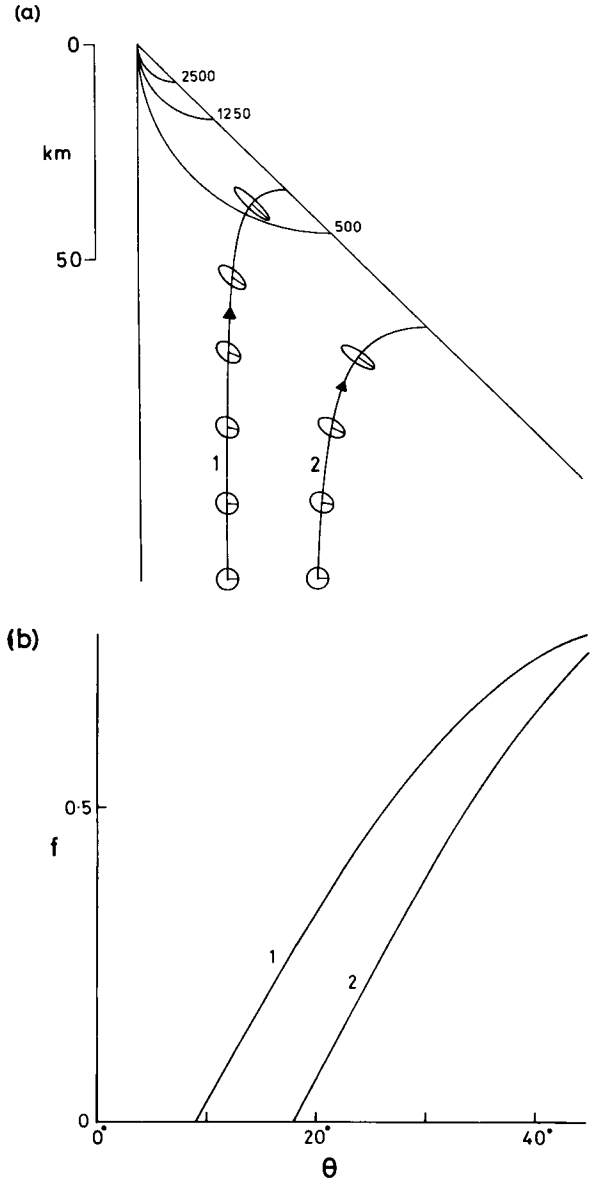

Figure 3. (a) Similarity solution for flow beneath a ridge, corresponding to (a) in Table 1. The circular fluid elements shown on the lower boundary are deformed into the ellipses as they move along the stream lines, shown as continuous curved lines with arrows in the flow direction. The straight line through the centre of the ellipse shows the orientation of a single vector in the fluid element at successive times. To the right of the oblique line rigid motion occurs. The curved lines passing through the origin are contours of the stress field, marked with the stress in bars, for a viscosity of 10^{22} poise (10^{21} Pa s) and a half spreading rate v_x = 20 mm/yr. The horizontal and vertical scale is shown on the left. (b) The finite strain $f = \log_{10}(a/b)$, where a and b are the semimajor and semiminor axes of the strain ellipse respectively, along the two stream lines shown in (a), marked 1 and 2.

Section 2. The first case shown in Fig. 3 corresponds to flow beneath a ridge. The integration starts with a unit matrix at the lowest point shown on each stream line and continues until $\theta = \alpha$. In this and all other examples below $\mathscr{F}(t)$ is used to obtain the shape which a circle, drawn in the fluid at $t = 0$, would have at this time. The straight line joining

the stream line to the ellipse at each time shows the orientation of one vector at various times. The contours of shear stress $\sigma_{r\theta}$ in this and other similarity solutions are shown, obtained from

$$\sigma_{r\theta} = \eta|\omega|/r \tag{46}$$

where η is the viscosity, taken to be 10^{22} poise (10^{21} Pa s). In Fig. 3(a) each stream line passes through a region where the deformation is most rapid shortly before it reaches $\theta = \alpha$. This is also shown in Fig. 3(b) where f is shown as a function of θ. For both stream lines f increases monotonically with θ until $\theta = \alpha$. The total deformation and orientation of the ellipses in Fig. 3(a) are similar for both of these and for other stream lines. This result is a consequence of the importance of the rapid deformation near $\theta = \alpha$, and not of equation (45), since the initial values of θ are different. These results show that substantial extension ($a/b \simeq 6$) occurs and this and similar plots show that the long axes of the resultant ellipses are in all cases subparallel to $\theta = \alpha$ where the stream lines cross this line.

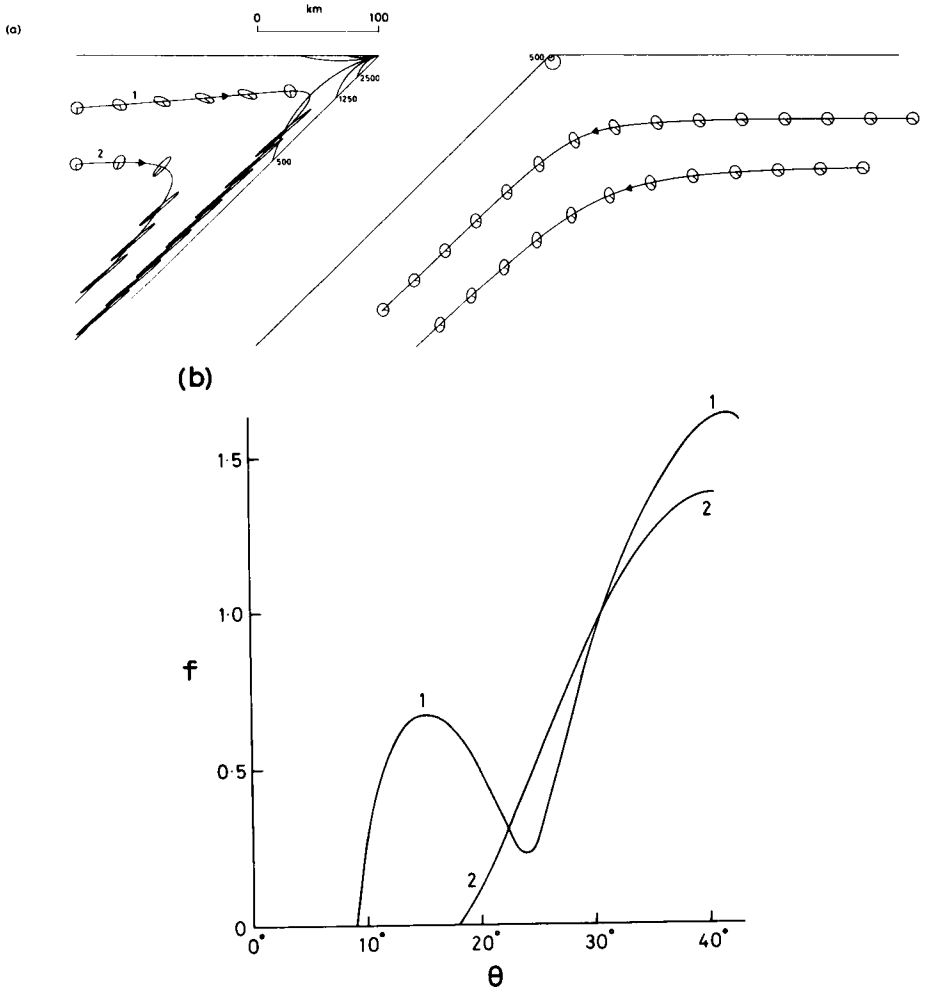

Figure 4. (a) Similarity solutions for the flow above and below a sinking slab when the upper surface of the region above the slab is fixed (Table 1, cases (c) and (d)). The convergence velocity v_r is 100 mm/yr and the stress contours are in bars (see Fig. 3). (b) The finite strain along the two stream lines in (a) which are above the sinking slab.

The trench model shown in Fig. 4 has $\mathbf{v} = 0$ on the upper surface above the sinking slab. The deformation beneath the sinking slab is rather weak, but that above it exceeds $f = 1.5$ ($a/b \simeq 30$). Fig. 4(b) shows that f only increases monotonically with θ on stream line 2. On stream line 1 f has two maxima. This behaviour is caused by the existence of a region near the surface where the maximum extension direction is approximately at 90° to the direction in the region near the slab. The fluid element is therefore first stretched to form an ellipse, then later stretched more strongly in a direction approximate parallel to the short axis of the ellipse formed during the first part of the deformation. The long axes of the ellipses near the slab are approximately parallel with its upper boundary. If the surface above the sinking slab is stress free rather than fixed the behaviour of the deformation is similar. The stress ellipses are orientated subparallel to the sinking slab, but $f(\theta)$ is slightly smaller and contains only one maximum.

From the geophysical point of view the most important result is that large strains are produced in the region above sinking slabs regardless of the surface boundary conditions. These strains are produced near the region where the material on each stream line is subject to the greatest shear stress. The direction of maximum extension is approximately parallel to the sinking slab. The deformation beneath the sinking slab is relatively small compared with that above. The number of cases for which calculations were carried out was considerably larger than those shown here, and demonstrated that the results were not strongly dependent on α. Although the strain increased as α decreased, the orientation of the ellipses was little affected.

5 Strain in convecting fluids

The original purpose of this investigation was to understand the deformation of fluid elements in a vigorously convecting fluid. Since the stream function for such circulation must be obtained numerically so must $\mathscr{F}$, using the methods discussed in Section 2. The stream functions used were those obtained by McKenzie, Roberts & Weiss (1974) for convection with free boundaries, and some new solutions obtained with rigid upper and lower boundaries on which the velocity vanishes.

Fig. 5 shows the behaviour of one fluid element in convecting fluid whose Raleigh number is 1.4×10^6, with upper and lower boundaries stress free and all the heat supplied from below (see McKenzie *et al.* 1974, figure 18 for details). The deformation of a fluid element, represented by a circle at position 1 in Fig. 5(a) and an ellipse at later times, is substantial. The orientation of the greater principal axis of the ellipse shows little relationship to the direction of maximum instantaneous extension. This complicated behaviour is the result of the rapid rotation of any radius of the circle in a frame fixed to the direction of instantaneous maximum extension. It is clear from geometric considerations that the direction maximum extension must change by an angle of $n\pi$, where n is an integer and the angle measured in a laboratory frame, when a fluid element describes any closed curve (Fig. 5(b)). In Fig. 5(a) n is 2. The rotation of a fluid element is more complicated and is controlled by the vorticity. Unlike the similarity solutions, where vorticity diffuses in from the boundaries, that in Fig. 5 is generated by horizontal temperature gradients within the fluid. The dimensionless relationship is (McKenzie *et al.* 1974)

$$\nabla^2 \omega = \partial_x T \tag{47}$$

and the free boundary conditions require $\omega = 0$ on all boundaries. The path of the fluid element is shown superimposed on the vorticity in Fig. 5(c), and it is clear from (a) that the total rotation of a vector during one overturn is substantial. The geometry of the flow imposes a constraint on this rotation. Since stream lines cannot cross, and since they are

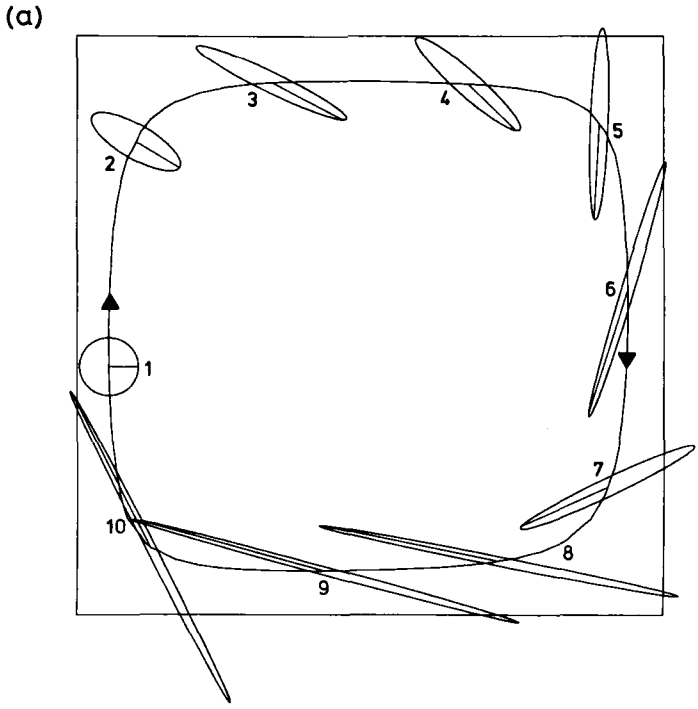

Figure 5. (a) Deformation within a convecting fluid with a Rayleigh number of 1.4×10^6 and driven by heat supplied from below. All boundaries are stress free (see McKenzie *et al.* 1974; figure 18). Both sides of the square are 700 km. The position marked 1 is at a depth of 400 km where the deformation is taken to be zero, due to the phase change from spinel or olivine. The stream line shown is that with dimensionless stream function $\psi' = -0.1$. The deformation ellipses are at equally spaced intervals in time of 11.9 Myr. The straight line through their centres shows the orientation of one vector in the fluid element at different times. (b) Stream line in (a) superimposed on vectors whose direction is that of the greatest instantaneous extension direction and whose length is proportional to the extension rate. (c) Stream line in (a) superimposed on the dimensionless vorticity. The contour interval is 1.0 and the vorticity is zero on the boundaries of the box. (d) The finite strain f as a function of time in Myr for the stream line in (a). (e) The length of the vectors shows the magnitude of the finite strain f at 24 Myr, and their direction is that of semimajor axis of the strain ellipse.

particle paths if the flow is steady, points on the circle initially in the interior part of the cell cannot cross the stream line. Hence in one overturn all vectors must rotate through angles between π and 3π, and the two vectors tangential to the stream line must remain so throughout the motion, rotating through 2π. The rotation for all vectors is in the opposite sense to that of the maximum extension direction. From the discussion in Section 3 this rapid rotation should produce an oscillation in f, and this is shown in Fig. 5(d). Because the environment of the element changes rapidly, f does not return to zero. In this case f can be approximately described by a harmonic oscillation superimposed on a linear trend, but in general the behaviour is more complicated. One feature of Fig. 5(d) which is easily explained is the linear trend. Once the ellipse is strongly flattened, shortening in almost all directions will cause this flattening to increase. It is unlikely (although not impossible) that later shortening will return the ellipse to a circle. This argument depends on the general tendency of disorder to increase in complicated non-linear physical systems. The superimposed oscillation in f is produced by the rotation between the ellipse and the extension direction, and is easily seen by comparing Fig. 5(a) with Fig. 5(d). The behaviour of elements on other stream lines (Fig. 6) is similar, although the deformation decreases strongly towards the

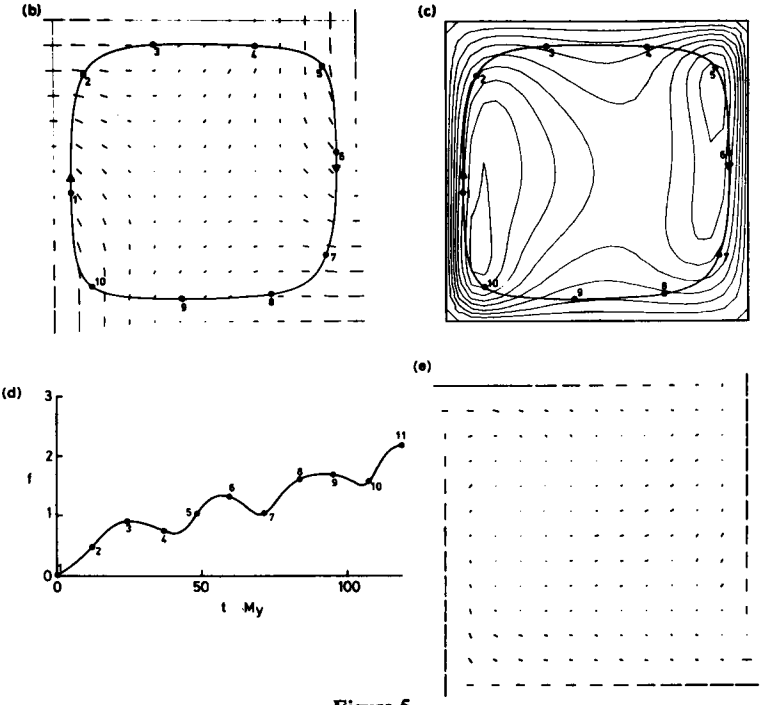

Figure 5

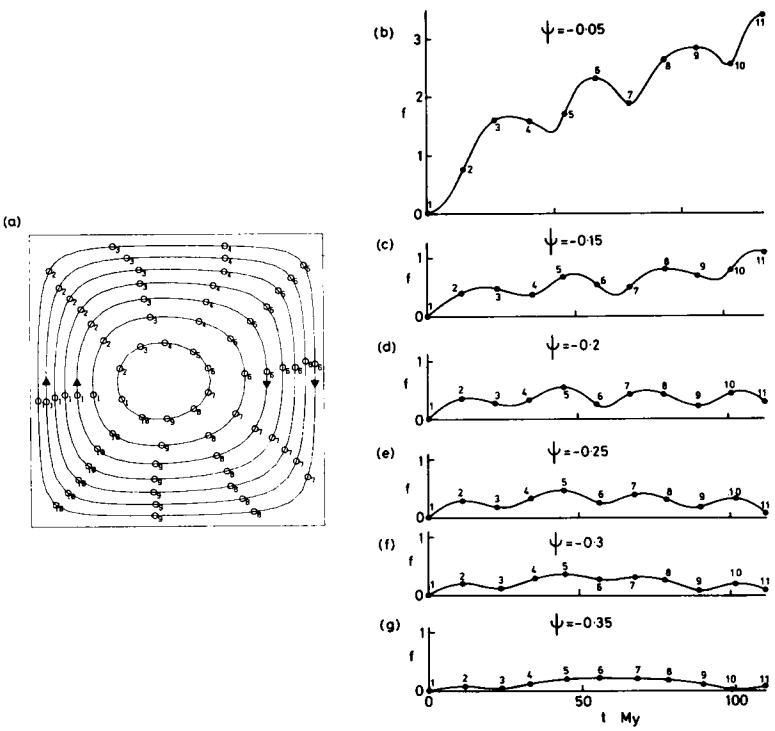

Figure 6. (a) Stream lines for the convective flow in Fig. 6. Contour interval is 0.05 and $\psi' = 0$ on the boundary of the box. (b)–(g) The finite strain f for all the stream lines in (a) except that shown in Fig. 5(d). (b) is for the outermost stream line, (g) for that in the centre. Because the overturn time varies with the stream line the time interval between successive points on different stream lines is not the same.

centre of the cell. The interior of two-dimensional convection cells at large Rayleigh number is a region where the vorticity varies little (Fig. 5(c)). This region, therefore, rotates in a manner similar to that of a solid cylinder, with little internal deformation. Such solid body rotation also causes the circulation time of each element to vary little with position (Fig. 6), and produces small finite strains in the interior. The magnitude and orientation of the finite strain throughout the fluid at 24 Myr in Fig. 5(e) shows the same behaviour, and, because of the advection of finite deformation by the flow, differs considerably from the

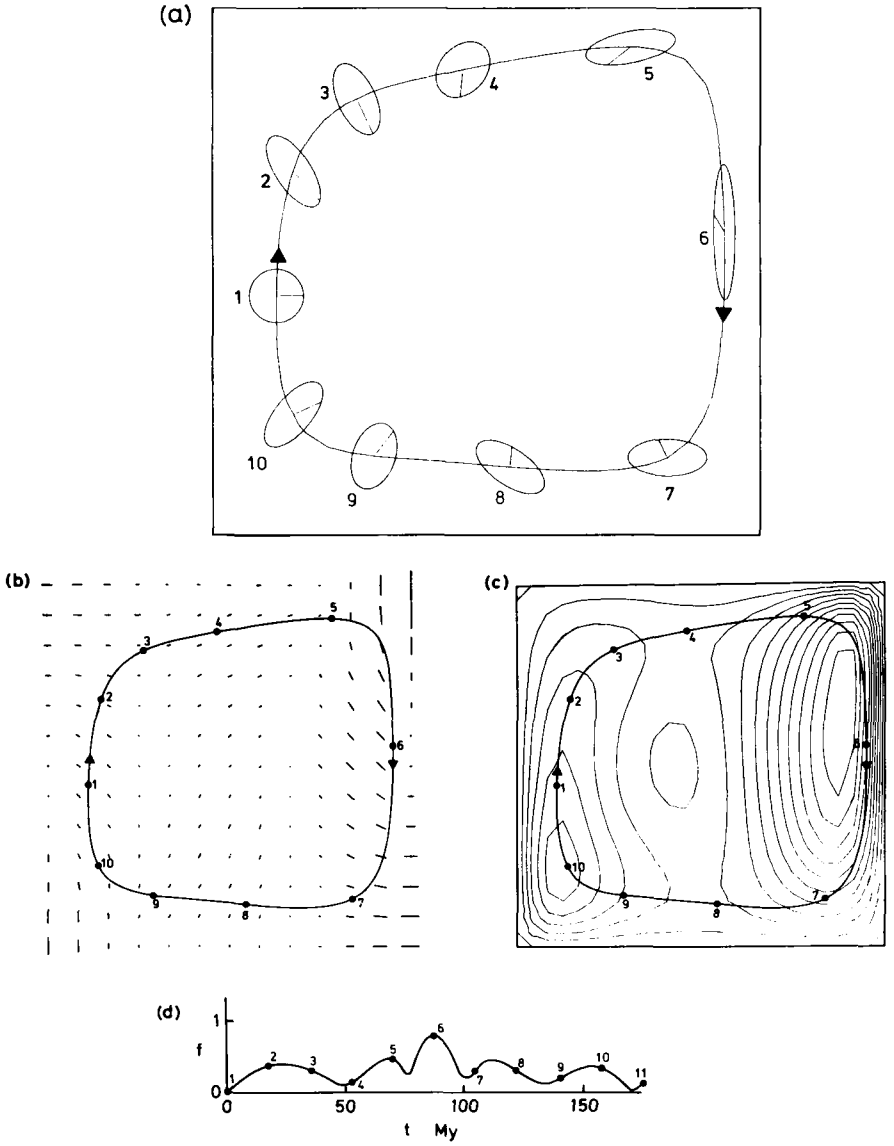

Figure 7. (a) Deformation within a convecting fluid with the same Rayleigh number and stress boundary conditions as in Figs 5 and 6, but with half the heat supplied by internal heating. The stream line is that for $\psi' = -0.1$ and the time interval between successive ellipses is 17.4 Myr. (b)–(d) Correspond to 5(b)–(d) and show the instantaneous direction of maximum extension rate, the vorticity and the finite strain for (a) respectively.

corresponding plot of the instantaneous extension direction. On the edges of the region the deformation consists of pure shear whose rate depends on position. Because the vorticity is zero on these boundaries the finite strain accumulates faster than it does elsewhere. This rather simple behaviour in the interior of the fluid is a consequence of the absence of internal heat generation, which generates vorticity in the interior and prevents solid body rotation. If the upper and lower boundaries are fixed, the form of the flow is changed considerably. The velocities are considerably decreased, and each element takes about twice as long to describe each stream line. However, the vorticity and strain rate are increased, hence the finite strain is also. There is no region in the centre of the cell where the vorticity is constant, although presumably one would develop if the Rayleigh number was increased. Hence the finite strain produced during one overturn is considerable, even on stream lines far from the boundaries.

Convection driven partly or entirely by internal heating does not possess an interior region where the vorticity is constant (Fig. 7(c)). The reason for this difference is that most of the vorticity generation in Fig. 5(c) occurs close to the rising sheets of hot fluid and the sinking sheets of cold fluid, where the horizontal temperature gradients are large. When heat is produced in the interior of the fluid so are horizontal temperature gradients. Fig. 7(a) shows the finite deformation produced on a stream line within a convection cell driven half by internal heating and half by heating from below, with the same Rayleigh number of 1.4×10^6 as that used in Fig. 5. There is a considerable difference between the total deformation in Figs 5(a) and 7(a). This difference is not the result of changes in the strain rate, but occurs because on this stream line the rotation produced by the vorticity is matched to that of the maximum direction of extension. Deformation on stream lines on both sides of that in Fig. 7(a) is considerably larger (Fig. 8(b), (d)), and the decrease towards the centre of the cell is less than that in Fig. 6.

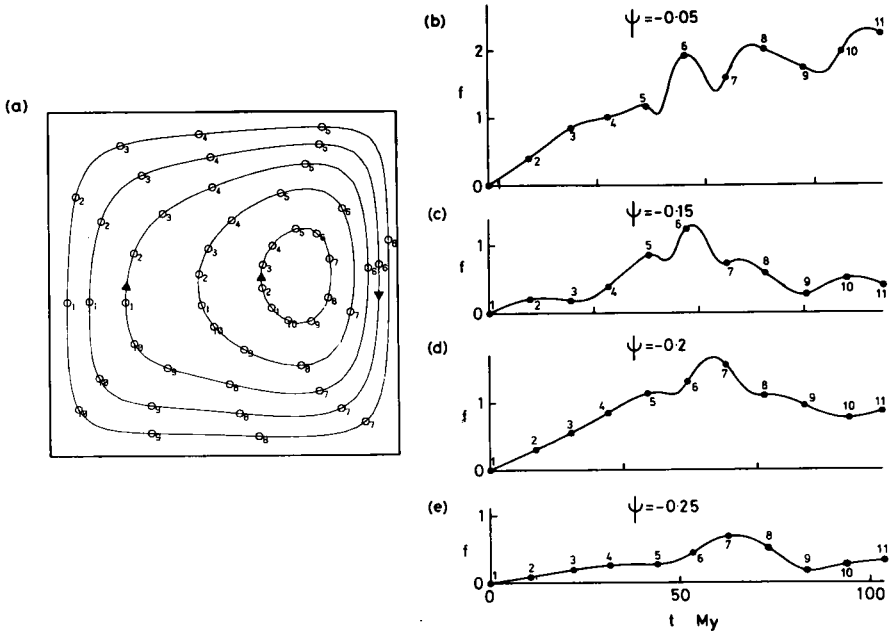

Figure 8. (a) Contours of the stream function at 0.05 unit intervals for the flow in Fig. 7. ((b)–(e) finite strain for the stream lines in (a), except that in Fig. 7(d). (b) is for the outermost curve, (e) for that near the centre.

A number of other cases were examined with Rayleigh numbers of 2.4×10^4 and 2.4×10^5. The magnitude of f after one overturn differed little from that in Figs 5–8, although at low Rayleigh numbers there is no constant vorticity region in the cell interior, even when the heat is supplied from below. Therefore the interior region is more deformed than that in Fig. 6. Temperature-dependent viscosity also had little effect.

It is clear from the remarks above that thermal convection produces complicated finite strain, which varies rapidly with position, and that the simpler problems discussed in Sections 3 and 4 are of limited help in understanding the detailed behaviour.

6 The relation between finite strain and fabric

The finite deformation of a fluid element can be observed directly if some object whose initial shape is known is introduced at a known time. This is the method used by most tectonic geologists to determine the finite strain (see Ramsay 1967). If care is taken to use markers which deform in the same way as the fluid, this method can give $\mathscr{F}(t)$ when the deformation is complete, but not that at intermediate times. Unfortunately there are no known markers in the mantle which can be used for this purpose. The only information which is available comes from preferred orientation of minerals, which can either be measured directly if samples are available, or indirectly by measuring the seismic anisotropy. Other details of the crystal fabric, such as the grain and sub-grain size or the dislocation density, are more sensitive to the last phase of deformation, especially if this took place under large stresses. Since all emplacement of mantle material has involved a high stress phase during extraction from the mantle and emplacement in the crust, and since this phase is not related directly to the motions beneath the plates, we shall only consider the influence of finite deformation on mineral orientations.

The relationship between deformation and crystal orientation has generated considerable controversy (see Nicolas & Poirier 1976 and Williams 1977 for recent reviews). Some authors (Kamb 1959; Ave'Lallement & Carter 1970) have argued on thermodynamic grounds that crystal orientation is controlled by the stress field, and hence by the symmetric part $\mathscr{S}$ of the velocity gradient tensor. On general grounds this argument seems unlikely. The density of small structures, such as dislocations, in a crystal depends on the past history of the crystal and never reaches thermodynamic equilibrium. It is hard to believe that the rotation of a whole crystal can be controlled by thermodynamic forces, and especially difficult to believe that this process can align the crystals when externally imposed rotation is also occurring. Furthermore crystal orientation can only occur through some form of creep, and this often involves dislocations. Thermodynamic theories ignore the contribution of these dislocations to the internal energy of the crystals, whereas studies of grain growth during recovery in metals suggest that this energy strongly influences grain growth (see Nicolas & Poirier 1976). One particularly important experiment was carried out by Kamb (1972) who deformed ice in simple shear. He found that the resulting fabric had monoclinic symmetry, and therefore could not have been produced by the stress field. He argued that the velocity gradient tensor did have the required symmetry and that his experiments were not consistent with thermodynamic control.

The alternative view which is now widely accepted is that the orientation is related to the finite strain. Evidence in favour of this model is discussed by Williams (1977) and by Ramsay (1967). In olivine Nicolas *et al.* (1971) have observed that the [010] direction (Fig. 9) is aligned normal to the shear plane in simple shear, whereas the [100] axis is aligned in the shear direction. Therefore in this example the [010] axis is aligned along the direction of greatest shortening, the [100] along that of greatest extension. The same relationship between strain and crystal orientation will align [010] along σ_1, the greatest principal stress,

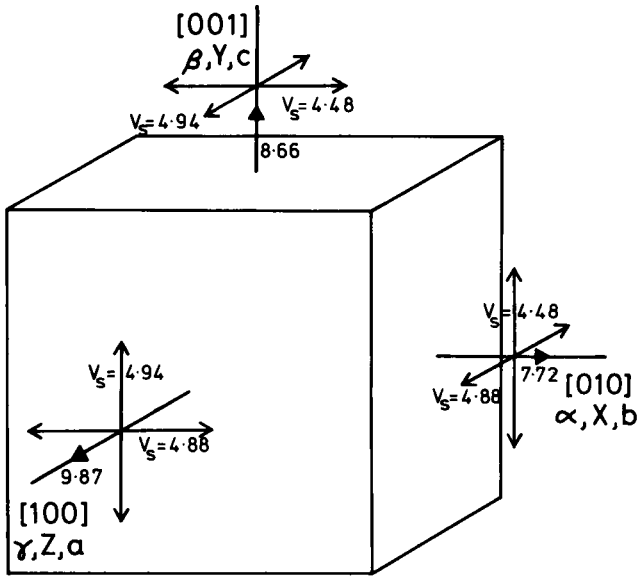

Figure 9. *P* and *S* velocities along the three principal axes of an olivine crystal. The velocities and those in Fig. 10 were obtained by Keith (private communication) from the constants listed by Verma (1960), and differ by as much as 1.5 per cent from those measured by Verma. Four different crystallographic notations commonly used are indicated. In this paper we assume that [100] is aligned along the axis of greatest finite strain, and [010] along the axis of least strain.

when the deformation is carried out in pure shear (Ave'Lallement & Carter 1970). Nicolas, Boudier & Boullier (1973) argue that the orientation results from intracrystalline glide, but grain growth during high temperature recovery could also be important. Fortunately the mechanism is not of major importance to the present argument. As Carter (1976) has emphasized all mechanisms which have been proposed only occur when the creep is dominated by the movement of dislocations.

The relationship between the axes of the finite strain ellipse and the orientation of olivine crystals will be used in the discussion below, but it is difficult to believe that the fabric is independent of the time history of $\mathcal{F}(t)$. Available experiments are, however, little help in understanding what the relationship might be, even for metals. The strain needed to produce a strong fabric was found to be $f \gtrsim 0.4$ in olivine (Nicolas *et al.* 1973) when creep occurs through dislocation climb at high temperatures (1200–1300°C). Because of recrystallization the shape of individual crystals after deformation cannot be used to estimate f.

As has already been mentioned all olivine fabrics which have been studied in the field are believed to be the result of dislocation motions (see Nicolas & Poirier 1976). Hence the stress must be sufficiently large to mobilize the dislocations at mantle temperatures. The stress which must be applied before the creep is dominated by dislocation movement is very uncertain. For such discussions it is convenient to define a normalized stress by

$$\Sigma = \log_{10}(\sigma/\mu) \tag{48}$$

where $\mu (= 7.9 \times 10^{11}$ dyne cm^{-2}, 7.9×10^{10} Pa) is the shear modulus. The lowest estimate is that of Weertman (1970) of 10^{-2} bar (1 kPa, $\Sigma = -7.9$). Stocker & Ashby (1973) carefully examined all available data on olivine and believed about 7 bar (0.7 MPa, $\Sigma = -5.05$) was the best estimate. McKenzie (1968) collected the results of a number of experiments on

ceramics and thought 50 bar (5 MPa, $\Sigma = -4.3$) was a reasonable value, whereas Twiss (1976) has recently used a modification of diffusion creep proposed by Ashby & Verrall (1973) to give estimates as large as 200 bar (20 MPa, $\Sigma = -3.6$). Of these values that of Stocker & Ashby (1973) is probably too low because they did not consider the contribution of grain boundary sliding in the diffusion creep regime. Twiss' (1976) estimate is strongly influenced by his belief that post-glacial observations require the mantle to deform as a Newtonian fluid, and that dislocation creep does not occur. Although Peltier & Andrews (1976) and Cathles (1975) have demonstrated that the observations can be fitted by a Newtonian model with some accuracy, no systematic investigations have yet been made of non-Newtonian ones. Hence it is not yet clear what constraints these observations place on mantle rheology. Although this question will probably be resolved by experiments, large strains at low stresses are necessary and are not easily produced.

A preferred crystal orientation once formed is not easy to destroy. Diffusion creep of the type proposed by Nabarro (1948), Herring (1950) and Coble (1963) leaves the crystal orientations unchanged, and deformation at higher stresses produces a new orientation in a different direction. Two processes appear to be able to destroy the fabric. The first and most obvious is phase changes. The change from cubic spinel to orthorhombic olivine structure occurs at a depth of about 400 km in the rising fluid, and for this reason the integrations in Section 5 were started at this depth. Although recrystallization to a phase of different symmetry is likely to destroy most of the fabric, the process may not be complete because there may be a preferred orientation between the two phases which allows grain boundaries to migrate rapidly (Ashby, private communication). Such complications will be ignored. The other process which can destroy a fabric is diffusion creep by grain boundary sliding (Ashby & Verrall 1973). This deformation mechanism causes grain rotation, and the preferred orientation is gradually lost. Ashby (private communication) estimates that strains of $f \gtrsim 2$ will be required to remove a strong fabric.

An obvious objection to using any of the results from Sections 4 and 5 to discuss crystal orientation is that all the calculations were carried out for a Newtonian fluid, and are only strictly valid if dislocation motions do not dominate the flow. However, recent calculations by Paramentier, Turcotte & Torrance (1976) have demonstrated that the flows are scarcely affected if a realistic power law relationship is used instead of the Newtonian laws. Hence the finite strain behaviour must also be largely unaffected by the change in rheology. If power law creep does occur and produces a strong fabric the relationship between stress and strain rate will be anisotropic. Whether this effect will be important depends on the creep anisotropy. Durham, Goetze & Blake (1977) studied the deformation of single olivine crystals at high temperatures, and showed that dislocations climbed as fast as they slipped at low stresses. Goetze (private communication) argued that this behaviour suggested that creep anisotropy is unlikely to be important in the upper mantle even where the rock has a strong fabric.

In summary then we will assume that the effect of finite straining is to orient the [010] axis of olivine along the direction of greatest shortening and the [100] axis along that of greatest extension, provided the finite strain f exceeds 0.4 and the normalized stress Σ exceeds -5. For the reasons discussed these are at present reasonable assumptions, but are likely to be changed somewhat by future work.

7 Seismic anisotropy and xenolith fabrics

The only method available at present for observing the orientation of crystals in the mantle is seismic anisotropy. Hess (1964) pointed out that the velocity of the mantle beneath the

Moho obtained from refraction surveys in the Pacific depended on the azimuths of the lines. The velocity normal to the fracture zones is less than that measured parallel to them. Hess suggested that the shear which produced the fracture zones also orientated the olivine crystals. This explanation is no longer generally accepted because the shearing associated with transform faults is believed to be localized, and the observed offsets are generally inherited from earlier ridge geometries and are never produced by global shear fields. Hess' suggestion stimulated a number of careful refraction experiments (Raitt *et al.* 1969; Morris, Raitt & Shor 1969; Keen and Barrett 1971; Keen & Tramontini 1970) which have strongly confirmed the original observations. The fast direction is approximately normal to the magnetic anomalies, and the difference in velocity between the fast and slow directions varies from 0.2 to 0.6 km/s. Since the upper 20 to 30 km of the oceanic plate behaves elastically over long time-scales (10^7yr or more) any anisotropy must be produced where the plates are formed beneath a spreading ridge. Francis (1969) proposed a model for mantle emplacement which aligned the [010] axis vertically and the [100] axis horizontally and normal to the magnetic lineations (Fig. 10(a)). The deformation process which he believed produced this alignment was not examined in detail. Peselnick, Nicolas & Stevenson (1974) took oriented specimens from an ultramafic body which possessed the crystal fabric proposed by Francis and showed that the velocity anisotropy of this model compared well with that observed. Fountain (1976) has carried out similar experiments with similar results, although he did not find a strong orientation of [010]. The similarity solution in Fig. 3 can produce the orientation proposed by Francis provided α is large and boundary 2 in Fig. 2 is inclined at a small angle to the horizontal (Fig. 10). Under these conditions the upwelling region which produces the plates must be broad. The stresses are sufficiently large to

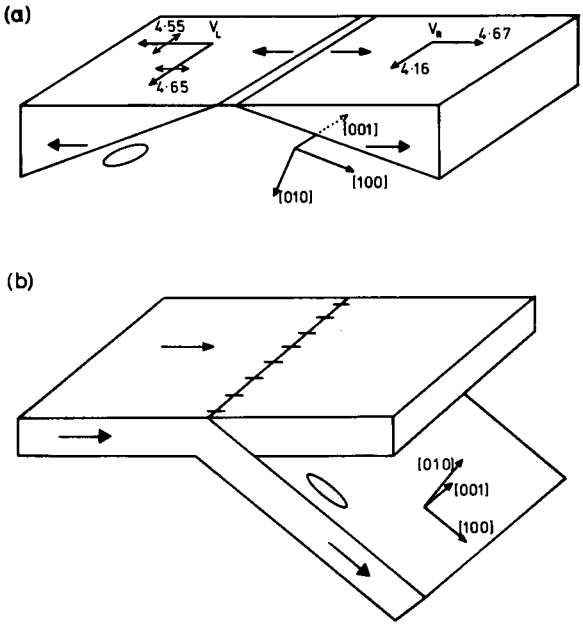

Figure 10. (a) Sketch to show the crystal orientation produced by a spreading ridge when the dip of the base of the lithosphere is small. The Rayleigh-wave velocities V_R in km/s shown apply if the [010] axis is vertical and the [001] axis is parallel to the ridge. They therefore neglect the dip of the lithosphere. The Rayleigh wave and Love wave velocities V_L shown are the limiting velocities for long-period waves, and in the case of Love waves the velocity is that of *SH* waves. (b) Corresponding sketch to (a) for the region above the sinking slab.

activate dislocation climb. As fluid elements move along the stream lines they lose heat to the surface. Since the deformation rate depends exponentially on temperature, creep will cease as the fluid cools through a small temperature range, and the resulting fabric will thereafter be frozen in. Hence rapidly spreading ridges with large values of α should produce fabrics with [100] closer to the horizontal than slow spreading ones (Fig. 10(a)), and therefore with large and more easily observed seismic anisotropy. Of the observations mentioned above only that of Keen & Tramontini (1970) was made on a slow spreading ridge, and this example was also the least convincing. The model also predicts that there should be a large anisotropy for *SV* propagating horizontally, but much less for *SH* (Fig. 10). The mean velocity of *SH* should be considerably larger than that for *SV*. These effects are in the right sense to account for the small surface wave anisotropy found by Forsyth (1975, 1977) and by Schlue & Knopoff (1976). However, the small velocity variations observed by these authors could have other origins.

Processes beneath ridges are easier to investigate than those near island arcs because spreading processes control the structure of oceanic lithosphere. However, Fig. 4 shows that the strain induced by subduction above the sinking slabs is much larger than that beneath ridges, and should produce important anisotropy with the fastest *P* direction [100] parallel to the sinking slab (Fig. 10(b)). High velocities in this plane have been observed in most island arcs but, after the general acceptance of plate tectonics, have been attributed to thermal effects rather than crystal orientation. Earlier suggestions by Sugimura & Uyeda (1966) and by Cleary (1967) that anisotropy could be involved should be re-examined. The most obvious method to use is the *P*-wave velocity of waves propagating above the slab and parallel to the arc. This velocity should be large if the anomaly is thermal but not if it is due to anisotropy.

The most likely form the small-scale flow will take is that illustrated in Fig. 7. Unlike the similarity solutions, such flow does not produce regions where the strain ellipses have constant shape and orientation. Therefore the anisotropy will not be easily detected by seismic techniques.

Some xenoliths in lavas and kimberlite pipes equilibrated at depths up to 200 km. Therefore some of these xenoliths were originally part of the convecting mantle beneath the plates and potentially provide information about the creep processes involved. There are, however, two major problems in using fabric observations obtained from studies of the nodules. Obviously no information is available about their orientation before extraction. The other difficulty concerns the process by which they were extracted, which probably involved a steadily increasing stress field imposed at high temperatures. How much of the fabric results from creep during the local processes associated with the generation of the kimberlite or lava is unclear. This creep is not relevant to the general mantle circulation. Hence the most interesting nodules from the point of view of mantle circulation are those which show least deformation, called protogranular by Mercier & Nicolas (1975) when they occur in basalts, or coarse granular in kimberlites (Boullier & Nicolas 1975). These xenoliths show little preferred orientation of either the olivine or enstatite crystals. They do show some signs of high-temperature deformation by dislocation movement, but the strains involved are small. The important question is whether this fabric can be produced by recrystallization of a severely strained rock, as Harte, Cox & Gurney (1975) have suggested. If their suggestion is correct then fabric observations on xenoliths cannot yet provide any constraints on the rheology of general mantle motions. However, Boullier & Nicolas (1975) believe that the minor phases in the xenoliths would still be dispersed as small grains if the olivine had recrystallized, and found no such distribution. The type of mantle circulation now believed to be occurring everywhere beneath the plates produces extensive finite strain throughout

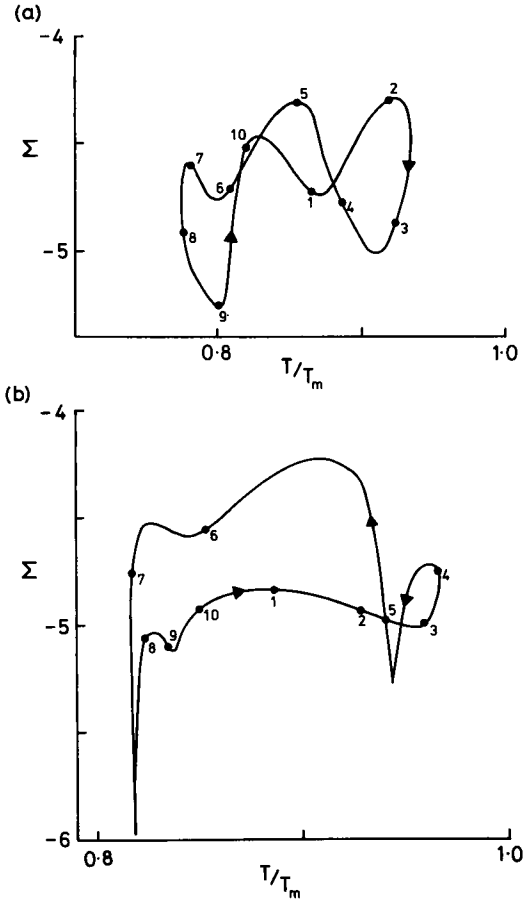

Figure 11. Paths which fluid elements follow as they describe the stream line in Fig. 5(a), (a), and that in Fig. 7(a), (b). The vertical axis shows $\Sigma = \log_{10}(\sigma/\mu)$ where σ is the shear stress and μ is the shear modulus, plotted as a function of $(T + T_r)/T_M$, where $T_r = 1070 + 700(1 - z/d)$ is a reference temperature in °K and T_M the melting temperature. Both T_M and μ were taken to be functions of depth. $T_M = 1470 + 1100(1 - z/d)$, $\mu = 6.7 \times 10^{11} + 8.3 \times 10^{11}(1 - z/d)$ dyne cm^{-2} $= 6.7 \times 10^{10} + 8.3 \times 10^{10}(1 - z/d)$ Pa.

the fluid in 10^8yr or less. If we accept Boullier & Nicolas' (1975) argument, the crystals in all xenoliths should be oriented if dislocation climb has been important. Hence the weakly deformed fabrics are only compatible with the models discussed in Section 5 if diffusion creep is important. The paths of two fluid elements in plots of Σ against T/T_M are shown in Fig. 11 for the same stream lines discussed in Figs 5 and 7. These paths can be used to estimate lower bounds on the stress at which dislocation climb becomes important. If this stress is much less than $\Sigma = -4.5$ (25 bar, 2.5 MPa) xenoliths without a strong fabric should be very rare. Although available laboratory experiments do not yet provide good estimates of the stress at which this transition occurs, this estimate is compatible with present limited knowledge (see Section 6). If this estimate is correct considerable deformation will occur in parts of the mantle without producing any fabric. The most important such region is the low-viscosity zone which Richter & McKenzie (1978) argued decouples the motions of plates from that of the mantle below. If the thickness of this zone is 50 km and the plate velocity is 100 mm/yr, strains of $f = 1$ are produced in 1.5 Myr, although the

stresses involved are less than 5 bar (0.5 MPa). The creep mechanism will probably be that of Ashby & Verrall (1973) and should combine grain boundary sliding with diffusion. This process will rapidly produce a random fabric even if the initial orientation is strong.

It might perhaps have been expected that the stresses involved in mantle convection would be close to those required for dislocation climb. Power law creep can be described by an effective viscosity which is a strongly decreasing function of stress. Hence the convective velocity increases more rapidly with increasing buoyancy force when the flow is governed by power law creep than when it is controlled by Newtonian creep. This effect will tend to stabilize the stress in the convecting fluid close to the transition stress. This conjecture should obviously be tested by numerical experiments.

8 Geochemistry

Since diffusion is unimportant in the mantle on scales greater than a few metres, the ellipses in Figs 5 and 7 show the shape a small closed system will have after one overturn. The deformation in the third dimension will probably be even more severe because of the large-scale circulation associated with the plate motions. Hence a closed system is rapidly stretched into a large thin sheet. This behaviour is not properly described as mixing since closed systems remain closed until the deformation is sufficiently extreme for diffusion to become important. For instance, if a sphere of diameter 50 km is placed at position 1 in Fig. 5(a), after one overturn the longer axis of the resulting ellipse will be about 600 km, the shorter about 4 km. Although surprisingly little is known about the geometry of magma sources, a source the shape of this ellipse is implausible. Hence on a time-scale of 10^8 yr convection will produce sufficient deformation to resemble mixing. Since the large-scale flow involved in plate movements is time dependent, all parts of the upper mantle are mixed by changes in plate geometry. The only region which may not be involved in this mixing is the mantle below a depth of about 700 km.

This argument in favour of a well-mixed mantle is not compatible with geochemical evidence. Surprisingly large variations have now been clearly demonstrated in the $^{87}Sr/^{86}Sr$ (Hart, Schilling & Powell 1973), the lead isotope (Sun, Tatsumoto & Schilling 1975), and the $^{143}Nd/^{144}Nd$ (O'Nions, Hamilton & Evenson 1977) ratios. The only model which appears able to explain some of these variations is the plume model of Schilling (1973), which depends on the lower mantle acting as a separate geochemical system from the upper mantle. O'Nions, Pankhurst & Grönvold (1976) have, however, argued that a mixing model cannot account for all the observed ratios with only two systems. Furthermore the widespread nature of the anomalies requires a large number of plumes, and the small scale of the necessary motions seems unlikely. The only other obvious explanation is that the anomalous ratios are produced by the rather complicated dynamic melting which must occur beneath spreading ridges, and which is poorly modelled by the simple geochemical models usually considered.

9 Discussion

The relationship between the Eulerian velocity field and finite deformation obtained in Section 2 should be useful in a variety of problems in structural geology. Since the relevant quantities are easily obtained from numerical solutions, rather general problems can be investigated. The simple deformation investigated in Section 3 illustrates the importance of rotation or vorticity in finite deformation, and shows the relationship between pure shear, simple shear and flows where the vorticity is even more important. The deformation which

occurs in these flows differs in important ways from that which occurs in more realistic circulations with lower symmetry. In the flows examined in Sections 4 and 5 the finite deformation generally increases with time, but, because of rotation, complicated oscillations also occur. The similarity solutions discussed in Section 4 are relevant to the circulation beneath ridges and trenches, and can produce the seismic anisotropy observed in oceanic plates. The calculations also suggest that anisotropy will occur above sinking slabs, with the fast *P*-wave velocity oriented parallel to the dip of the slab. Fast *P*-wave velocities in such regions are well known, but have previously been attributed to thermal effects, rather than to anisotropy. Clearly further investigations are required to determine the importance of these two effects.

Finite deformation in most convective circulations occurs throughout the fluid, not only in those parts which move close to the boundaries. Because of vorticity generation in the interior, the deformation produces no large regions with constant orientation, and therefore will be difficult to study using *P*-wave velocities. In Section 7 it is argued that the weakly deformed nodules are more relevant to mantle deformation than the strongly deformed ones on which more work has been done. Some of these weakly deformed xenoliths must come from the asthenosphere, where the calculated finite strains are large. Hence the weak deformation suggests that diffusion creep is important in mantle circulation. Dislocation climb must, however, dominate in regions of high stress.

The large finite strains strongly deform geochemically closed regions. Although real mixing can only occur by diffusion, magma generation from a closed region will be difficult. Hence the chemistry of the magma, but perhaps not that of the nodules, should reflect strong and rapid mixing.

The main shortcoming of this investigation is produced by our ignorance of the relationship between large complicated finite strains and the resulting crystal orientation and other microstructure of the rock. Investigation of ice in glaciers and ice sheets (Hambrey 1977) would be very valuable, since both the strain fields and the fabrics are more easily investigated than are those of the mantle.

Acknowledgments

I am grateful to Ben Harte for interesting me in the fabric of kimberlite nodules and starting this investigation. I would also like to thank Michael Ashby, Frank Richter, Keith O'Nions, Colum Keith and Jay Melosh for helpful suggestions and references, and Colum Keith for calculating the velocities in Fig. 10. Jean Hewitt carried out some of the numerical calculations. The work was completed at Lamont-Doherty Geological Observatory while the author was a senior post-doctoral fellow, and forms part of a general investigation of mantle convection supported by the NERC at Cambridge.

References

Ashby, M. F. & Verrall, R. A., 1973. Diffusion accommodated flow and superplasticity, *Acta Metall.*, **21**, 149.

Ave'Lallement, H. G. & Carter, N. L., 1970. Syntectonic recrystallization of olivine and modes of flow in the upper mantle, *Bull. Geol. Soc. Am.*, **81**, 2203.

Batchelor, G. K., 1967. *An Introduction to Fluid Dynamics*, Cambridge University Press.

Boullier, A. M. & Nicolas, A., 1975. Classification of textures and fabrics of peridotite xenoliths from South African kimberlites, *Phys. Chem. Earth*, **9**, 97.

Carter, N. L., 1976. Steady state flow of rocks, *Rev. Geophys. Space Phys.*, **14**, 301.

Cathles, L. M., 1975. *The Viscosity of the Earth's Mantle*, Princeton University Press.

Cleary, J., 1967. Azimuthal variation of the Longshot source term, *Earth planet. Sci. Lett.*, **3**, 29.

Coble, R. L., 1963. A model for boundary diffusion controlled creep in polycrystalline materials, *J. Appl. Phys.*, **34**, 1679.

Dieterich, J. H. & Onat, E. T., 1969. Slow finite deformations of viscous solids, *J. geophys. Res.*, **74**, 2081.

Durham, W. B., Goetze, C. & Blake, B., 1977. Plastic flow of oriented single crystals of olivine 2. Observations and interpretations of dislocation structures, *J. geophys. Res.*, **82**, 5755.

Elliott, D., 1972. Deformation paths in structural geology, *Bull. Geol. Soc. Am.*, **83**, 2621.

Forsyth, D. W., 1975. The early structural evolution and anisotropy of the oceanic upper mantle, *Geophys. J. R. astr. Soc.*, **43**, 103.

Forsyth, D. W., 1977. The evolution of the upper mantle beneath mid-ocean ridges, *Tectonophys.*, **38**, 89.

Fountain, D. M., 1976. The Ivrea–Verbano and Strona–Ceneri zones, northern Italy: a cross-section of the continental crust – new evidence from seismic velocities of rock samples, *Tectonophys.*, **33**, 145.

Francis, T. J. G., 1969. Generation of the seismic anisotropy in the upper mantle along mid-ocean ridges, *Nature*, **221**, 162.

Hambrey, M. J., 1977. Foliation, minor folds and strain in glacier ice, *Tectonophys.*, **39**, 397.

Hart, S. R., Schilling, J.-G. & Powell, J. L., 1973. Basalts from Iceland and along the Reykjanes Ridge: Sr isotope geochemistry, *Nature Phys. Sci.*, **246**, 104.

Harte, B., Cox, K. G. & Gurney, J. J., 1975. Petrography and geological history of upper mantle xenoliths from Matsoku kimberlite pipe, *Phys. Chem. Earth*, **9**, 617.

Herring, C., 1950. Diffusional viscosity of a polycrystalline solid, *J. Appl. Phys.*, **21**, 437.

Hess, H. H., 1964. Seismic anisotropy of the uppermost mantle under the oceans, *Nature*, **203**, 629.

Hobbs, B. E., Means, W. D. & Williams, P. F., 1976. *An Outline of Structural Geology*, J. Wiley, New York.

Jaegar, J. C., 1962. *Elasticity, Fracture and Flow*, 2nd edn, Methuen, London.

Kamb, W. B., 1959. Theory of preferred crystal orientation developed by crystallization under stress, *J. Geol.*, **67**, 153.

Kamb, B., 1972. Experimental recrystallization of ice under stress, in *Flow and Fracture in Rocks*, ed. Heard, H. C. *et al.*, American Geophysical Union Monograph 16.

Keen, C. & Tramontini, C., 1970. A seismic refraction survey on the Mid-Atlantic Ridge, *Geophys. J. R. astr. Soc.*, **20**, 473.

Keen, C. E. & Barrett, D. L., 1971. A measurement of seismic anisotropy in the Northeast Pacific, *Can. J. Earth Sci.*, **8**, 1056.

Lachenbruch, A. H., 1976. Dynamics of a passive spreading center, *J. geophys. Res.*, **81**, 1883.

Malvern, L. E., 1969. *Introduction to the Mechanics of a Continuous Medium*, Prentice-Hall, Englewood Cliffs, New Jersey.

McKenzie, D. P., 1968. The geophysical importance of high temperature creep, in *The History of the Earth's Crust*, ed. Phinney, R. L., Princeton University Press.

McKenzie, D. P., 1969. Speculations on the consequences and causes of plate motions, *Geophys. J. R. astr. Soc.*, **18**, 1.

McKenzie, D. P., Roberts, J. M. & Weiss, N. O., 1974. Convection in the Earth's mantle: towards a numerical simulation, *J. Fluid Mech.*, **62**, 465.

Mercier, J.-C. C. & Nicolas, A., 1975. Textures and fabrics of upper-mantle peridotites as illustrated by xenoliths from basalts, *J. Petrology*, **16**, 454.

Morris, G. B., Raitt, R. W. & Shor, G. G., 1969. Velocity anisotropy and delay-time maps of the mantle near Hawaii, *J. geophys. Res.*, **74**, 4300.

Nabarro, F. R. N., 1948. *Deformation of Crystals by Motion of Single Ions*, p. 75, Rep. Conf. Strength Solids, Bristol.

Nicolas, A., Bouchez, J. L., Boudier, F. & Mercier, J.-C. C., 1971. Textures, structures and fabrics due to solid state flow in some European lherzolites, *Tectonophys.*, **12**, 55.

Nicolas, A., Boudier, F. & Boullier, A. M., 1973. Mechanisms of flow in naturally and experimentally deformed peridotites, *Am. J. Sci.*, **273**, 853.

Nicolas, A. & Poirier, J. P., 1976. *Crystalline Plasticity and Solid State Flow in Metamorphic Rocks*, J. Wiley, London.

O'Nions, R. K., Hamilton, P. J. & Evenson, N. M., 1977. Variations in $^{143}Nd/^{144}Nd$ and $^{87}Sr/^{86}Sr$ in oceanic basalts, *Earth planet. Sci. Lett.*, **34**, 13.

O'Nions, R. K., Pankhurst, R. J. & Grönvold, K., 1976. Nature and development of basalt magma sources beneath Iceland and the Reykjanes Ridge, *J. Petrology*, **17**, 315.

Parmentier, E. M., Turcotte, D. L. & Torrance, K. E., 1976. Studies of finite amplitude non-Newtonian thermal convection with application to convection in the Earth's mantle, *J. geophys. Res.*, **81**, 1839.

Parsons, B. & McKenzie, D. P., 1978. Mantle convection and the thermal structure of the plates, *J. geophys. Res.*, **83**, 4485.

Peltier, W. R. & Andrews, J. T., 1976. Glacial-isostatic adjustment I: the forward problem, *Geophys. J. R. astr. Soc.*, **46**, 605.

Peselnick, L., Nicholas, A. & Stevenson, P. R., 1974. Velocity anisotropy in a mantle peridotite from the Ivrea zone: Application to the upper mantle anisotropy, *J. geophys. Res.*, **79**, 1175.

Raitt, R. W., Shor, G. G., Francis, T. J. G. & Morris, G. B., 1969. Anisotropy of the Pacific upper mantle, *J. geophys. Res.*, **74**, 3095.

Ramsay, J. G., 1967. *Folding and Fracturing of Rocks*, McGraw-Hill, New York.

Richter, F. & McKenzie, D. P., 1978. Simple plate models of mantle convection, *J. Geophys.*, **44**, 441.

Schilling, J.-G., 1973. Icelandic mantle plume: geochemical study of the Reykjanes Ridge, *Nature*, **242**, 565.

Schlue, J. W. & Knopoff, L., 1976. Shear wave anisotropy in the upper mantle of the Pacific basin, *Geophys. Res. Lett.*, **3**, 359.

Stocker, R. L. & Ashby, M. F., 1973. On the rheology of the upper mantle, *Rev. Geophys. Space Phys.*, **11**, 391.

Sugimura, A. & Uyeda, S., 1966. A possible anisotropy of the upper mantle accounting for deep earthquake faulting, *Tectonophys.*, **5**, 25.

Sun, S. S., Tatsumoto, M. & Schilling, J.-G., 1975. Mantle plume mixing along the Reykjanes Ridge: lead isotopic evidence, *Science*, **190**, 143.

Twiss, R. J., 1976. Structural superplastic creep and linear viscosity in the Earth's mantle, *Earth planet Sci. Lett.*, **33**, 86.

Verma, R. K., 1960. Elasticity of some high-density crystals, *J. geophys. Res.*, **65**, 757.

Weertman, J., 1970. The creep strength of the Earth's mantle, *Rev. Geophys. Space Phys.*, **8**, 145.

Williams, P. F., 1977. Foliation: a review and discussion, *Tectonophys.*, **39**, 305.